Quantifying Uncertainty in Deck Deflections from Distributed Fiber Optic Strain Data

Patrick Brewick
Assistant Professor, Dept. of Civil and Environmental Engineering & Earth Sciences, Univ. of Notre Dame, Notre Dame, IN, USA

ABSTRACT: A naval hovercraft was outfitted with a distributed fiber optic sensing system (FOSS) on its cargo deck in which two fibers were placed along orthogonal axes. A series of trucks were loaded onto the cargo deck and the resulting strain profiles were measured. The aim of this study is to quantify the deck deflections that correspond to measurements taken under operational loading. This is accomplished by idealizing the cargo deck as a rectangular plate and using the data to estimate the associated plate model parameters. In order to account for measurement noise and model prediction error, as well as the inherent variability of inferences made with different data sets, a hierarchical Bayesian scheme that considers both the model parameter uncertainty and the prediction error variance is utilized. Through this hierarchical Bayesian formulation, the posterior distributions of the model parameters are found, and from these distributions, deck deflection envelopes are created and compared to service limit deflections.

1. INTRODUCTION

The fiber optic sensor system (FOSS) has emerged as a potentially powerful tool for conducting structural health monitoring (Glisic and Inaudi, 2008) via strain sensing of marine structures (Kageyama et al., 1998; Majewska et al., 2014). For instance, Fiber Bragg grating (FBG) sensors, one type of FOSS, have been increasingly utilized for strain measurements in hull monitoring systems (Wang et al., 2001; Kim et al., 2012; Shen et al., 2015). The growing utilization of FOSS for marine health monitoring applications is due to a few primary factors. First, recent advances in fiber optic technology have led to distributed sensing solutions within a single fiber (Murayama et al., 2011), wherein a single fiber contains hundreds to thousands of sampling points. In distributed sensing, fiber gratings are regularly placed all along the length of a fiber, up to several meters, creating a high density of sampling points within a single "sensor." These fiber gratings do not measure strain directly, rather they only allow a specified wavelength to be reflected, *e.g.*, a Bragg wavelength, while transmitting all others. When subjected to deformation, such as an applied strain field, any changes in the longitudinal axis of the fiber are registered as shifts in the Bragg wavelength, and these shifts are directly related back to strain information.

A FOSS also offers a robust means of measuring strain in harsh environments, as optical fiber is insensitive to electro-magnetic interference, resistant to corrosion, and capable of operating across a wide range of temperatures (Murayama et al., 2003). This allows optical fiber to be reliably outfitted in a variety of locations and geometrical patterns on a structural platform. These qualities make fiber well-suited to provide measurements on marine craft, where complex geometries are common and measurement equipment is regularly subjected atmospheric and environmental stressors capable of severely damaging many traditional sensing technologies.

Strain data produced by FOSS can be used to infer additional response information for a given structure, such as stress fields and displacements. The inverse finite element method (iFEM) (Vazquez et al., 2005) has been utilized for shape and stress sensing from FOSS data on both aerospace (Tessler, 2007) and marine (Kefal and Oterkus, 2015) platforms. While iFEM has demonstrated flexibility across structural topologies, it requires intimate knowledge of the exact structural geometry, and that information is not always available. Analytical methods have also been successfully used for inferring deflections from FOSS strain data, including curve-fitting (Kim and Cho, 2004) and least-squares based approaches (Shkarayev et al., 2001). These methods offer the advantage of using only a few parameters, as well as appropriate theory from engineering mechanics, to describe the response of a given structure.

In contrast to previous deterministic analytical approaches, this study adopts a Bayesian framework for inferring deflections from FOSS strain data. This study utilizes a low-order analytical model to quantify the deflection response of the cargo deck of the Landing Craft Air Cushion (LCAC) hovercraft due to service loads, where the model is calibrated through a hierarchical Bayesian approach (Sedehi et al., 2019). The LCAC is a kind of air-cushioned vehicle (hovercraft) employed by the United States Navy as a means of transport for personnel, equipment, and cargo. As such, the LCAC serves a variety of crucial purposes but also requires in-depth service life evaluations, including exploration of the deflections experienced by the deck during a variety of loading conditions. However, these measurements can only be collected through field testing, which introduces a greater degree of uncertainty than if measurements were collected in a controlled laboratory environment. This study attempts to account for these uncertainties through the application of a hierarchical Bayesian approach, provide more robust predictions of the global deck deflections and, thus, better quantify the associated uncertainties.

2. BACKGROUND

2.1. *Craft Instrumentation*

Two distributed sensing fiber cables with approximately 1 cm grating spacing were placed in orthogonal directions along the cargo deck of an LCAC,

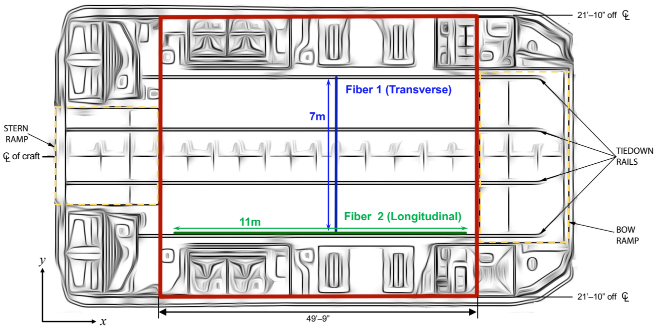

Figure 1: Cargo deck of an LCAC including cable locations and "main span" considered for the plate model.

as shown in Figure 1. Taken together, these two cables provide wavelength shifts along two primary axes, allowing for the creation of a two-dimensional strain field. The raw measurement data, *i.e.*, wavelength shifts, from both fibers were post-processed, resulting in 2 cm spatial resolution with an accuracy of ± 1 nm — which equates to ± 0.85 microstrain — collected at a 1 s refresh rate (or 1 Hz sampling rate).

2.2. *Testing*

Testing was designed to capture structural behavior of the cargo deck under normal operational loading conditions, as shown in Table 1. During testing, large vehicles of known weight, such as medium tactical vehicle replacements (MTVRs) and high mobility multipurpose wheeled vehicles (HMMWVs), were driven onto the deck and then driven off again after remaining stationary for 30-60 s. During these tests the trucks were always positioned such that the loading was balanced about the centerline of the cargo deck, *e.g.*, single trucks straddled the centerline while two trucks were approximately symmetrical about the centerline. In addition, vehicle engines remained on, subjecting the deck to low-amplitude mechanical vibrations. Table 1 lists the tests conducted in which Fibers 1 and 2 were actively measuring the strain response.

3. MODEL

This study focuses on the area of the craft bounded by the edges on either extreme along the y-axis and the ramps at the bow and the stern along the x-axis (indicated by dashed boxes in Figure 1). This area, highlighted by a bold box in Figure 1,

Table 1: Description of truck test loadings.

Test No.	Vehicles	Weight
A01	1 MTVR	34,600 lbs
A03	1 MTVR	34.600 lbs
A08	1 HMMWV	11,250 lbs
A09	1 HMMWV	11,250 lbs
A10	2 MTVRs	34,600 lbs; 38,687 lbs
A11	2 MTVRs	34,600 lbs; 38,687 lbs

includes the entirety of both fibers and is herein referred to as the "main span" of the deck.

3.1. Defining the plate model

This study applies Kirchoff plate theory to solve for the deflections of the main span, treating it as one large continuous plate whose thickness is much smaller than either length dimension.

The general equation for the bending deflection of a plate subjected to an arbitrary transverse load $f(x,y)$ is given by (Timoshenko and Woinowsky-Krieger, 1987)

$$\frac{\partial^4 w}{\partial x^4} + 2\frac{\partial^4 w}{\partial x^2 \partial y^2} + \frac{\partial^4 w}{\partial y^4} = \frac{f(x,y)}{D} \tag{1}$$

where w describes the displacement of the plate in the vertical direction, x and y are rectangular coordinates (shown with respect to the cargo deck in Figure 1), $\frac{\partial w}{\partial s}$ indicates a partial derivative of w taken with respect to s, and D is the flexural rigidity. Herein, the term "plate" will be taken as synonymous with the "main span" identified in Figure 1.

The strain experienced by the plate can be derived from the solution to Equation 1 through curvature relations as

$$\varepsilon_x = -z\frac{\partial^2 w}{\partial x^2} \qquad \varepsilon_y = -z\frac{\partial^2 w}{\partial y^2}. \tag{2}$$

where ε_s denotes the strain in the s direction at a vertical distance z from the neutral surface, and $\frac{\partial^2 w}{\partial s^2}$ denotes the curvature with respect to the sz plane. The z-direction (vertical deflection) is assumed to be positive in the downward direction in Equation 2.

3.2. Truck loading

For the purposes of the model, the weight of a truck is treated as a series of point loads p at the given wheel locations, such that

$$f(x,y) = \sum_{i=1}^{n_{\mathrm{wh}}} p_i\, \delta(x-\xi_i)\delta(y-\eta_i) \tag{3}$$

where n_{wh} is the number of wheels for a given vehicle, $\delta(\cdot)$ is the Dirac delta function, and (ξ_i, η_i) are the coordinates of the ith wheel load.

Assuming linear behavior, Equation 3 can be plugged into Equation 1 as a forcing function. For a rectangular plate simply supported along all boundaries, the closed-form solution to the vertical deflection due to a series of point loads is

$$w_{\mathrm{point}} = \frac{4}{\pi^4 abD} \sum_{i=1}^{n_{\mathrm{wh}}} p_i \sum_{m}^{\infty}\sum_{n}^{\infty} \frac{\sin\frac{m\pi\xi_i}{a}\sin\frac{n\pi\eta_i}{b}}{\left(\frac{m^2}{a^2}+\frac{n^2}{b^2}\right)^2} \sin\frac{m\pi x}{a}\sin\frac{n\pi y}{b} \tag{4}$$

where a and b denote the dimensions of the plate in the x and y directions, respectively.

3.3. Boundary conditions

With respect to boundary conditions, the edges of the plate adjacent to the stern and bow ramps can be treated as simply supported because the beams supporting the deck (from underneath) provide vertical support without necessarily preventing rotation. Thus, $w = 0$ and $\frac{\partial^2 w}{\partial x^2} = 0$ at $x = 0$ and $x = a$. The boundaries along the port $y = b$ and starboard $y = 0$ sides exhibit a greater degree of rigidity due to increased structural supports and are more appropriately modeled as "clamped" boundaries.

However, a supporting element running along the centerline of the cargo deck (shown as an approximately dashed line parallel to x-axis in Figure 1) possesses sufficient stiffness to appear in the strain measurements. As such, this stiffener must be included for the model to properly reflect the structural response of the deck. To accomplish this, the main span is divided into two halves: one spanning $y = 0$ to $y = b_{\mathrm{h}}$, the other from $y = b_{\mathrm{h}}$ to $y = b$, where $y = b_{\mathrm{h}} = b/2$ is the centerline. In order to solve for the total deflection w_{tot} of the plate, the superposition principal must be applied as in

$$w_{\mathrm{tot}} = w_{\mathrm{tot}}^{S} + w_{\mathrm{tot}}^{P} \tag{5}$$

where w_{tot}^S and w_{tot}^P are the total displacement solutions for the starboard (S) and port (P) sides, respectively. Each side has its own respective version of Equation 5, as in

$$w_{\text{tot}}^j = w_{\text{point}}^j + w_{\text{elastic}}^j \tag{6}$$

where ^{j} is either S or P and w_{elastic} represents the solution for enforcing both the centerline stiffener and clamped boundaries along y-axis.

The solution to w_{elastic} takes the form (Timoshenko and Woinowsky-Krieger, 1987)

$$w_{\text{elastic}}^j = \sum_{k=1}^{\infty} Y_k^j \sin \frac{k\pi x}{a} \tag{7}$$

where

$$Y_k^j = A_k^j \cosh \frac{k\pi y}{a} + B_k^j \frac{k\pi y}{a} \sinh \frac{k\pi y}{a} + C_k^j \sinh \frac{k\pi y}{a} + D_k^j \frac{k\pi y}{a} \cosh \frac{k\pi y}{a}. \tag{8}$$

Coefficients A_k, B_k, C_k, D_k, are solved based on the appropriate boundary conditions using linear least squares. The stiffener is treated as an elastic foundation with unknown stiffness $EI_{\text{stiffener}}$, and the boundary conditions along either outer plate boundary remain as clamped. This produces the following set of boundary conditions for the starboard domain bounded by $y = 0$ and $y = b_{\text{h}}$:

$$\left. w_{\text{elastic}}^S \right|_{y=0} = 0 \tag{9a}$$

$$\left. \frac{\partial w_{\text{elastic}}^S}{\partial y} \right|_{y=0} = 0 \tag{9b}$$

$$\left. \left(\frac{\partial^2 w_{\text{elastic}}^S}{\partial y^2} + \nu \frac{\partial^2 w_{\text{elastic}}^S}{\partial x^2} \right) \right|_{y=b_{\text{h}}} = 0 \tag{9c}$$

$$D \left. \left[\frac{\partial^3 w_{\text{elastic}}^S}{\partial y^3} + (2-\nu) \frac{\partial^3 w_{\text{elastic}}^S}{\partial x^2 \partial y} \right] \right|_{y=b_{\text{h}}} = \left. \left(EI_{\text{stiffener}} \frac{\partial^4 w_{\text{elastic}}^S}{\partial x^4} \right) \right|_{y=b_{\text{h}}} \tag{9d}$$

where ν is Poisson's ratio for the plate.

For the port-side domain bounded by $y = b_{\text{h}}$ and $y = b$, continuity conditions are enforced along $y = b_{\text{h}}$. The continuity conditions ensure that the deflection and curvature of the plate remain continuous along the boundary formed by the elastic foundation. For the outer clamped boundary along $y = b$, $w_{\text{elastic}}^P = 0$ and $\frac{\partial w_{\text{elastic}}^P}{\partial y} = 0$ apply. Additional model details may be found in Brewick et al. (2022).

Table 2: Model parameters for the rectangular plate.

Name	Model Value	Description
a	1516.38 cm	length along x-axis
b	1330.96 cm	length along y-axis
h	18.42 cm	effective thickness
E	71×10^9 N/cm^2	Young's modulus
ν	0.33	Poisson's ratio

3.4. *Plate model parameters*

Gometric dimensions and material properties for the plate model are shown in Table 2. Note that an "effective" thickness is used for the model, as it accounts for closely-spaced stiffener beams seated immediately below the cargo deck without explicitly including them in the model. Material properties come from the standard values of aluminum alloys commonly used in naval applications.

The weights shown Table 1 are for the entire vehicle. This total weight was converted into point loads based on the number of wheels for the vehicle — six for the MTVRs, four for the HMMWVs — and then apportioned based on the approximate distribution of load in the vehicle. For the MTVRs, the two front wheels are each assigned ⅓ of the total weight/load and the back four tires are each apportioned an equal 1⁄12 share of the remaining load. For the HMMWVs, the front tires are also assigned ⅓ of the load, with the back tires each getting ⅙ of the remaining total. The wheel positions relative to the cargo deck, which dictate the point load coordinates (ξ_i, η_i), are determined from videos taken during testing.

In addition to $EI_{\text{stiffener}}$, the other primary unknown for the plate model is the flexural rigidity D. For a plate of uniform thickness, the flexural rigidity is typically given as $D = \frac{Eh^3}{12(1-\nu^2)}$. The presence of stiffening elements makes it such that the thickness of the cargo deck is not truly uniform; however, it is treated as uniform to limit the number of model parameters. Thus, the typical expression for D provides a useful initial approximation, but the "true" (or optimal) value of D is unknown. Similarly, the "true" value for $EI_{\text{stiffener}}$ in the elastic foundation is unknown, but the general dimensions of the support and its material properties provide an informed initial value.

4. BAYESIAN APPROACH

Assume that the plate model M can be described as $M(\boldsymbol{\theta})$, where $\boldsymbol{\theta}$ is a vector containing unknown model parameters D and $EI_{\text{stiffener}}$. The collected FOSS data can be represented by $\mathscr{D}$, which contains strain data from individual tests such that $\mathscr{D} = \{\mathscr{D}_i, i = 1,2,\ldots,N_{\mathscr{D}}\}$, where $N_{\mathscr{D}}$ is the number of test data sets. Each testing data set $\mathscr{D}_i$ contains corresponding strain measurements $\varepsilon_i(k\Delta l)$, where $k = 0,\ldots,n_{\mathrm{m}_i}$, Δl is the spacing between sensing points on the fiber of length l, and n_{m_i} is the total number of sensing points (strain measurements) in the ith data set. The prediction error, *i.e.*, the discrepancy between the measured strain data and the model-predicted outputs $\hat{\varepsilon}_i(k\Delta l,\boldsymbol{\theta})$ is defined as

$$e_i(k\Delta l,\boldsymbol{\theta}) = \varepsilon_i(k\Delta l) - \hat{\varepsilon}_i(k\Delta l,\boldsymbol{\theta}). \tag{10}$$

The uncertainty in the prediction errors, which arises from both modeling errors and measurement noise, can be described by a zero-mean multivariate Gaussian distribution with covariance matrix $\boldsymbol{\Sigma}$. Note that the variability across data sets allows $\boldsymbol{\theta}_i$ to correspond to $\mathscr{D}_i$ and $\boldsymbol{\Sigma}$ to be further defined as $\boldsymbol{\Sigma} = \{\boldsymbol{\Sigma}_i, i = 1,\ldots,N_{\mathscr{D}}\}$.

A hierarchical approach further expands the uncertainty of $\boldsymbol{\theta}$. In this case, uncertainty of $\boldsymbol{\theta}$ is modeled using a Gaussian distribution $N(\boldsymbol{\theta}|\boldsymbol{\mu_\theta},\boldsymbol{\Sigma_\theta})$ with uncertain parameters $\boldsymbol{\mu_\theta}$ and $\boldsymbol{\Sigma_\theta}$, which respectively denote the mean and covariance matrix. Thus, a hierarchical framework creates two classes of model parameters: the data-specific model parameters in $\boldsymbol{\theta}$ and the hyper-parameters $\boldsymbol{\mu_\theta}$ and $\boldsymbol{\Sigma_\theta}$. Put another way, model outputs $\hat{\varepsilon}_i(k\Delta l,\boldsymbol{\theta})$ are conditional on $\boldsymbol{\theta}_i$, while parameter vector $\boldsymbol{\theta}_i$ is conditional on hyper-parameters $\boldsymbol{\mu_\theta}$ and $\boldsymbol{\Sigma_\theta}$.

The joint distribution of all parameters, *i.e.*, parameters from both classes, can be updated according to data $\mathscr{D}$ through Bayes' rule as

$$p(\{\boldsymbol{\theta}_i\}_{i=1}^{N_{\mathscr{D}}},\{\boldsymbol{\Sigma}_i\}_{i=1}^{N_{\mathscr{D}}},\boldsymbol{\mu_\theta},\boldsymbol{\Sigma_\theta}|\mathscr{D}) \propto p(\mathscr{D}|\{\boldsymbol{\theta}_i\}_{i=1}^{N_{\mathscr{D}}},\{\boldsymbol{\Sigma}_i\}_{i=1}^{N_{\mathscr{D}}},\boldsymbol{\mu_\theta},\boldsymbol{\Sigma_\theta}) \, p(\{\boldsymbol{\theta}_i\}_{i=1}^{N_{\mathscr{D}}},\{\boldsymbol{\Sigma}_i\}_{i=1}^{N_{\mathscr{D}}},\boldsymbol{\mu_\theta},\boldsymbol{\Sigma_\theta}) \tag{11}$$

where $p(\{\boldsymbol{\theta}_i\}_{i=1}^{N_{\mathscr{D}}},\{\boldsymbol{\Sigma}_i\}_{i=1}^{N_{\mathscr{D}}},\boldsymbol{\mu_\theta},\boldsymbol{\Sigma_\theta}|\mathscr{D})$ represents the joint distribution, $p(\mathscr{D}|\{\boldsymbol{\theta}_i\}_{i=1}^{N_{\mathscr{D}}},\{\boldsymbol{\Sigma}_i\}_{i=1}^{N_{\mathscr{D}}},\boldsymbol{\mu_\theta},\boldsymbol{\Sigma_\theta})$ is the likelihood function $\mathscr{L}(\mathscr{D})$, and the prior probability is given by $p(\{\boldsymbol{\theta}_i\}_{i=1}^{N_{\mathscr{D}}},\{\boldsymbol{\Sigma}_i\}_{i=1}^{N_{\mathscr{D}}},\boldsymbol{\mu_\theta},\boldsymbol{\Sigma_\theta})$.

4.1. Implementation

The following is a highly condensed summary of the hierarchical approach put forward by Sedehi et al. (2019). Assuming that the data sets are statistically independent, along with the understanding that data set $\mathscr{D}_i$ only depends on $\boldsymbol{\theta}_i$ and $\boldsymbol{\Sigma}_i$ allows for the likelihood function to be simplified to $\mathscr{L}(\mathscr{D}) = \prod_{i=1}^{N_{\mathscr{D}}} p(\mathscr{D}_i|\boldsymbol{\theta}_i,\boldsymbol{\Sigma}_i)$. Based on this simplification, the likelihood for a given set of test data can further be defined in terms of its prediction errors, which are considered independent and identically distributed according to a zero-mean Gaussian distribution with prediction error variance $\boldsymbol{\Sigma}_i = \left(\sigma_e^{(i)}\right)^2$, yielding

$$\mathscr{L}(\mathscr{D}_i) = \prod_{k=1}^{n_{\mathrm{m}_i}} N\left(e_i(k\Delta l,\boldsymbol{\theta}_i)|0,\left(\sigma_e^{(i)}\right)^2\right) \tag{12}$$

The prior distribution from Equation 11 can be simplified by taking advantage of the independence of $\boldsymbol{\theta}_i$ and $\boldsymbol{\Sigma}_i$. Based on this, the distribution of hyper-parameters can be written as $p(\boldsymbol{\mu_\theta},\boldsymbol{\Sigma_\theta})$ while recalling that the prior for θ_i is defined as $N(\boldsymbol{\theta}_i|\boldsymbol{\mu_\theta},\boldsymbol{\Sigma_\theta})$. The prior distribution of $\boldsymbol{\Sigma}_i$ is not dependent on the hyper-parameters but instead determined by the prediction error variance. Using Jeffrey's non-informative prior to describe the prior distribution of the prediction error variance, and taking into account the simplifications above, allows for the joint prior distribution to be written as

$$p(\{\boldsymbol{\theta}_i\}_{i=1}^{N_{\mathscr{D}}},\{\boldsymbol{\Sigma}_i\}_{i=1}^{N_{\mathscr{D}}},\boldsymbol{\mu_\theta},\boldsymbol{\Sigma_\theta}) \propto p(\boldsymbol{\mu_\theta},\boldsymbol{\Sigma_\theta}) \prod_{i=1}^{N_{\mathscr{D}}} \left[\frac{N(\boldsymbol{\theta}_i|\boldsymbol{\mu_\theta},\boldsymbol{\Sigma_\theta})}{\left(\sigma_e^{(i)}\right)^2}\right] \tag{13}$$

The goal of the hierarchical Bayesian approach is to compute the posterior of the hyper-parameters, *i.e.*, $p(\boldsymbol{\mu_\theta},\boldsymbol{\Sigma_\theta}|\mathscr{D})$. This requires marginalizing the full joint posterior over the domains of $\boldsymbol{\theta}_i$ and $\boldsymbol{\Sigma}_i$. Following the work in Sedehi et al. (2019), marginalizing over $\boldsymbol{\Sigma}_i$ leads to

$$p(\{\boldsymbol{\theta}_i\}_{i=1}^{N_{\mathscr{D}}},\boldsymbol{\mu_\theta},\boldsymbol{\Sigma_\theta}|\mathscr{D}) \propto p(\boldsymbol{\mu_\theta},\boldsymbol{\Sigma_\theta}) \prod_{i=1}^{N_{\mathscr{D}}} \left[N(\boldsymbol{\theta}_i|\boldsymbol{\mu_\theta},\boldsymbol{\Sigma_\theta})\exp(-L_1(\boldsymbol{\theta}_i))\right] \tag{14}$$

where $L_1(\boldsymbol{\theta}_i)$ is given by the quantity

$$L_1(\boldsymbol{\theta}_i) = \frac{n_{\mathrm{m}_i}}{2} \ln \left[\sum_{k=1}^{n_{\mathrm{m}_i}} e_i(k\Delta l, \boldsymbol{\theta}_i)^2 \right] \qquad (15)$$

Sedehi et al. (2019) points out that for large n_{m_i}, $\exp(-L_1(\boldsymbol{\theta}_i))$ can be approximated by a Gaussian distribution such that $\exp(-L_1(\boldsymbol{\theta}_i)) \propto N(\boldsymbol{\theta}_i|\boldsymbol{\theta}_i^*, \boldsymbol{\Sigma}^*_{\boldsymbol{\theta}_i\boldsymbol{\theta}_i})$. The quantity $\boldsymbol{\theta}_i^*$ is computed via the minimization of $L_1(\boldsymbol{\theta}_i)$ and $\boldsymbol{\Sigma}^*_{\boldsymbol{\theta}_i\boldsymbol{\theta}_i}$ is defined as the inverse of the Hessian at $\boldsymbol{\theta}_i^*$, $[\nabla\nabla^{\mathrm{T}} L_1(\boldsymbol{\theta}_i^*)]^{-1}$.

Further marginalization over $\boldsymbol{\theta}_i$ yields the final expression for posterior of the hyper-parameters as

$$p(\boldsymbol{\mu}_{\boldsymbol{\theta}}, \boldsymbol{\Sigma}_{\boldsymbol{\theta}}|\mathscr{D}) \propto p(\boldsymbol{\mu}_{\boldsymbol{\theta}}, \boldsymbol{\Sigma}_{\boldsymbol{\theta}}) \prod_{i=1}^{N_{\mathscr{D}}} N(\boldsymbol{\mu}_{\boldsymbol{\theta}}|\boldsymbol{\theta}_i^*, \boldsymbol{\Sigma}_{\boldsymbol{\theta}} + \boldsymbol{\Sigma}^*_{\boldsymbol{\theta}_i\boldsymbol{\theta}_i}) \qquad (16)$$

4.2. *Estimating the model parameters*

It is important to consider that Equation 16 does not actually constitute the desired quantity in this case; the true intent is to find the posterior distribution of the model parameters according to $p(\boldsymbol{\theta}|\mathscr{D})$. This is achieved through an application of the total probability theorem and then integrating over the domain over the hyper-parameters, which can be numerically accomplished using Markov Chain Monte Carlo (MCMC) methods such that

$$p(\boldsymbol{\theta}|\mathscr{D}) \approx \frac{1}{N_{\mathrm{s}}} \sum_{m=1}^{N_{\mathrm{s}}} N(\boldsymbol{\theta}|\boldsymbol{\mu}_{\boldsymbol{\theta}}^{(m)}, \boldsymbol{\Sigma}_{\boldsymbol{\theta}}^{(m)}) \qquad (17)$$

where $\boldsymbol{\mu}_{\boldsymbol{\theta}}^{(m)}$ and $\boldsymbol{\Sigma}_{\boldsymbol{\theta}}^{(m)}$ are the mth samples drawn from $p(\boldsymbol{\mu}_{\boldsymbol{\theta}}, \boldsymbol{\Sigma}_{\boldsymbol{\theta}}|\mathscr{D})$ and N_{s} is the total number of samples.

4.3. *Robust predictions*

Let $\hat{w}_i(k\Delta l)$ represent the predicted deflection response for the ith test. Based on the full data set $\mathscr{D}$, a probabilistic model for the prediction deflection response can be approximate by

$$p\left(w_i(k\Delta l)|\mathscr{D}\right) \approx \frac{1}{N_{\mathrm{s}}} \sum_{m=1}^{N_{\mathrm{s}}} p\left(w_i(k\Delta l)|\boldsymbol{\theta}^{(m)}, \boldsymbol{\Sigma}_i\right). \qquad (18)$$

Note that Equation 18 can be computed according to only the parametric uncertainty in $\boldsymbol{\theta}$ by setting the prediction error variance term to zero. As previously noted, readers interested in a more thorough derivation and description of this approach should consult Sedehi et al. (2019).

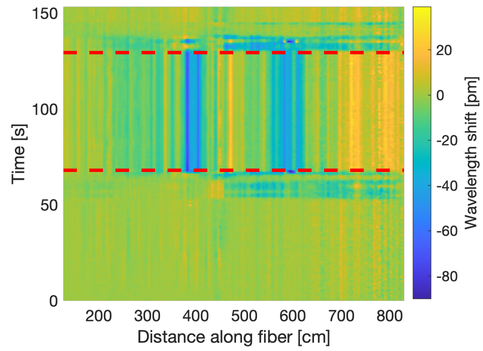

Figure 2: Wavelength shifts in Fiber 1 during Test A03.

5. RESULTS AND DISCUSSION

Figure 2 presents an example of the wavelength shifts measured along Fiber 1 during truck testing. The dashed lines in Figure 2 highlight the presence of the truck on the cargo deck, which is clearly visible within the plot. The model prediction error only considers this time window during which vehicles are present for a given test.

The hierarchical Bayesian approach is applied to the FOSS data from each truck test in a series of two steps. In the first step, a joint distribution of hyper-parameters is individually estimated for each truck test. This is accomplished by treating each time at which wavelength shift data is collected as a separate testing point; thus, for each test shown in Table 1 $N_{\mathscr{D}}$ is based on the number of measurements within the identified truck loading time window. By keeping the truck engines running during the tests, random process noise, in the form of mechanical vibrations, is introduced at each time instance in addition to the independent measurement noise. Therefore, the prediction error is probabilistically modeled as a zero-mean Gaussian distribution with a unique variance $\sigma^2_{e,i}$ at each time step.

In addition, since D and $EI_{\mathrm{stiffener}}$ potentially have values spanning several orders of magnitude, θ_D and θ_{EI} modify the initial values for D and $EI_{\mathrm{stiffener}}$, respectively, which are informed by the material property and geometry assumptions men-

Table 3: Statistics for θ_D and θ_{EI} from each truck test.

	θ_D		θ_{EI}	
Test No.	Mean	95% CI	Mean	95% CI
A01	0.531	[0.519,0.543]	3.676	[3.291,4.061]
A03	0.466	[0.461,0.471]	3.121	[3.055,3.187]
A08	0.251	[0.247,0.255]	5.465	[5.221,5.710]
A09	0.306	[0.292,0.321]	4.437	[4.314,4.560]
A10	0.467	[0.462,0.473]	0.999	[0.965,1.032]
A11	0.403	[0.399,0.406]	0.960	[0.954,0.966]

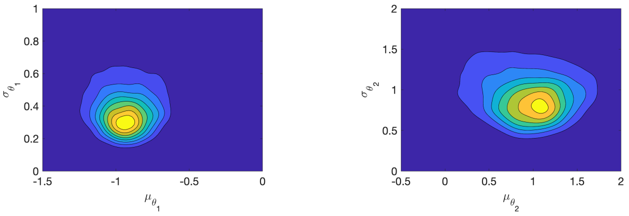

Figure 3: Posterior distribution of the hyper-parameters updated based on data from all truck tests.

tioned previously. Further, since both unknowns are stiffness quantities, log-normal random variables $\theta_1 = \ln(\theta_D)$ and $\theta_2 = \ln(\theta_{EI})$ are used to prevent any negative stiffness values. Thus, the parameter vector utilized within the Bayesian implementation is $\boldsymbol{\theta} = [\theta_1, \theta_2]$. Both θ_1 and θ_2 are assumed to follow Gaussian distributions $N(\theta_i|\mu_i, \sigma_i)$, where μ_i and σ_i are the hyper-parameters with uniform priors $\mu_i \sim U(-3,3)$ and $\sigma_i \sim U(0,3)$.

For the Bayesian implementation, a transitional Markov Chain Monte Carlo method (Wu et al., 2017) is used for generating samples, where $N_s = 10,000$. Statistics for the posterior distribution of θ_D and θ_{EI}, given by Equation 17, are provided in Table 3. These values demonstrate how much the model parameters change between tests; specifically, between loading types. The second step of the hierarchical Bayesian identification uses these values to estimate the joint distribution of θ_D and θ_{EI} considering data across all six truck tests, *i.e.*, the values in Table 3 are utilized as $\boldsymbol{\theta}_i^*$ within Equation 16 where $N_{\mathscr{D}} = 6$. For this step, the same priors are used for hyper-parameters considering the full data set. The resulting posteriors for the hyper-parameters are shown in Figure 3.

The ensuing final distributions for θ_D and θ_{EI} are shown in Figure 4, both of which appear to be log-normally distributed. The median values for these distributions are near-averages of the mean values from Table 3, but the variances are much larger, reflecting the increased uncertainty introduced when considering all of the data together. This significant increase in uncertainty is not surprising given the wide disparities in values in Table 3.

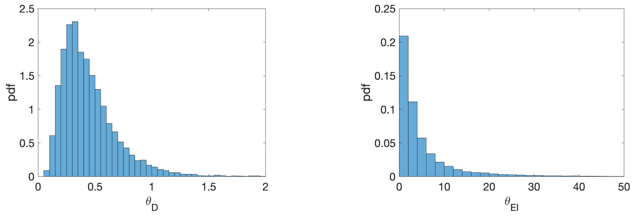

Figure 4: Final distributions for model parameters θ_D and θ_{EI} based on data from all truck tests.

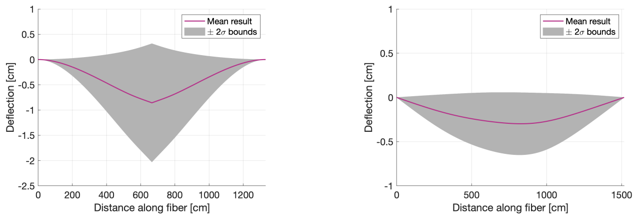

Figure 5: Sample deflection envelopes using model parameters updated based on data from all truck tests.

The final distributions for θ_D and θ_{EI} can be utilized with Equation 18 to provide more robust estimates of the deflections experienced during loading. A sample deflection envelope is shown in Figure 5. While the $\pm 2\sigma$ bounds in Figure 5 display rather large envelopes, the 99% confidence bounds on the maximum cargo deflections are within a reasonable service limit of 2.5 inches (6.35 cm) for each test.

6. CONCLUSIONS

A hierarchical Bayesian approach is applied to calibrating a low-parameter analytical model of a hovercraft cargo deck based on FOSS strain data. Adopting a hierarchical approach allows for the inclusion of both prediction error variance as well as uncertainty in the model parameters. The results showed that for individual loading tests on the hovercraft, the relative uncertainty in the model parameters was low, but when all testing data was taken together, the resulting variance was significantly larger. However, using this more inclusive methodology allowed for more robust predictions of the deflection responses that consider all sources of uncertainty. Even with the increased variance, the 99% confidence intervals of the deflections are below reasonable service limits. This is important because it allows for greater confidence in deriving deflections from FOSS data in the absence of additional instrumentation and with a limited number of available test data.

7. REFERENCES

Brewick, P. T., Wos, A. S., and Hutchinson, M. (2022). "Assessing the reliability of the cargo deck of a hovercraft through fiber optic strain measurements." *Marine Structures*, 81, 103090.

Glisic, B. and Inaudi, D. (2008). *Fibre optic methods for structural health monitoring*. John Wiley & Sons.

Kageyama, K., Kimpara, I., Suzuki, T., Ohsawa, I., Murayama, H., and Ito, K. (1998). "Smart marine structures: an approach to the monitoring of ship structures with fiber-optic sensors." *Smart Materials and Structures*, 7(4), 472.

Kefal, A. and Oterkus, E. (2015). "Structural health monitoring of marine structures by using inverse finite element method." *Analysis and design of marine structures*, C. G. Soares and R. A. Shenoi, eds., CRC Press/Balkema, GBR, 341–350.

Kim, N. S. and Cho, N. S. (2004). "Estimating deflection of a simple beam model using fiber optic bragg-grating sensors." *Experimental Mechanics*, 44(4), 433–439.

Kim, Y.-M., Lee, N.-K., Lee, S.-H., Bae, D.-M., and Yu, Y.-S. (2012). "Study on fbg sensors for hull stress monitoring." *Journal of Sensor Science and Technology*, 21(5), 276–282.

Majewska, K., Mieloszyk, M., Ostachowicz, W., and Król, A. (2014). "Experimental method of strain/stress measurements on tall sailing ships using fibre bragg grating sensors." *Applied Ocean Research*, 47, 270 – 283.

Murayama, H., Igawa, H., Omichi, K., and Machijima, Y. (2011). "Distributed sensing with ofdr and its application to structural health monitoring." *Proceedings of SPIE - The International Society for Optical Engineering*, 7753.

Murayama, H., Kageyama, K., Naruse, H., Shimada, A., and Uzawa, K. (2003). "Application of fiber-optic distributed sensors to health monitoring for full-scale composite structures." *Journal of Intelligent Material Systems and Structures*, 14(1), 3–13.

Sedehi, O., Papadimitriou, C., and Katafygiotis, L. S. (2019). "Probabilistic hierarchical bayesian framework for time-domain model updating and robust predictions." *Mechanical Systems and Signal Processing*, 123, 648–673.

Shen, W., Yan, R., Xu, L., Tang, G., and Chen, X. (2015). "Application study on fbg sensor applied to hull structural health monitoring." *Optik*, 126(17), 1499–1504.

Shkarayev, S., Krashantisa, R., and Tessler, A. (2001). "An inverse interpolation method utilizing in-flight strain measurements for determining loads and structural response of aerospace vehicles." *Proc. of the 3rd IWSHM*.

Tessler, A. (2007). "Structural analysis methods for structural health management of future aerospace vehicles." *Key Engineering Materials - KEY ENG MAT*, 347, 57–66.

Timoshenko, S. and Woinowsky-Krieger, S. (1987). *Theory of Plates and Shells*. McGraw-Hill, New York, 2nd edition.

Vazquez, S., Tessler, A., Quach, C., Cooper, E., Parks, J., and Spangler, J. (2005). "Structural health monitoring using high-density fiber optic strain sensor and inverse finite element methods." *Report No. TM-2005-213761*, NASA (06).

Wang, G., Pran, K., Sagvolden, G., Havsgård, G., Jensen, A., Johnson, G., and Vohra, S. (2001). "Ship hull structure monitoring using fibre optic sensors." *Smart materials and structures*, 10(3), 472.

Wu, S., Angelikopoulos, P., Papadimitriou, C., and Koumoutsakos, P. (2017). "Bayesian Annealed Sequential Importance Sampling: An Unbiased Version of Transitional Markov Chain Monte Carlo." *ASCE-ASME J Risk and Uncert in Engrg Sys Part B Mech Engrg*, 4(1).